Indian Journal of Pure & Applied Physics
Vol. 64, March 2026, pp. 251-259
DOI: 10.56042/ijpap.v64i3.22448

An Investigation of the Structural, Morphological, and Dielectric, Properties of $BiNi_{0.5}Se_{0.5}O_3$

P C Lalngilneia, Alok Shukla* & Sushil Joshi

Department of Physics, National Institute of Technology Mizoram, Aizawl 796 012, India

Received: 6th August 2025; accepted: 12th January 2026

The preparation and comprehensive analysis of the $BiNi_{0.5}Se_{0.5}O_3$ material, synthesized via a conventional solid-state route. Phase purity and crystallographic parameters were ascertained by powder X-ray diffraction, confirming the formation of the intended perovskite-type structure. Microstructural examination by scanning electron microscopy revealed a uniformly polycrystalline morphology, with grain sizes predominantly in the 3 μm range. Elemental composition and stoichiometry were verified through energy-dispersive X-ray spectroscopy, which demonstrated the presence of Bi, Ni, Se, and O in ratios consistent with the nominal formula. Dielectric permittivity and electrical conductivity measurements were performed over a broad spectrum of temperatures and frequencies. Analysis of impedance spectra indicates a pronounced negative temperature coefficient of resistance, attributable to contributions from both grain interiors and grain-boundary regions. The frequency-dependent conductivity follows Jonscher's universal power law, underscoring a hopping-dominated charge-transport mechanism. Collectively, these findings highlight $BiNi_{0.5}Se_{0.5}O_3$ as a promising candidate for next-generation electronic and energy-storage applications.

Keywords: Solid-state reaction, XRD, SEM, Dielectric

1 Introduction

Global efforts to develop sustainable energy technologies have highlighted ferroelectric ceramics for their spontaneous polarization below the Curie temperature, enabling applications from non-volatile memories to ultrasound transducers, actuators, and electro-optic modulators[1-4]. Perovskite oxides with the general formula ABO_3 are especially compelling: large A-site cations (e.g., Pb^{2+}, Bi^{3+}, Ba^{2+}, Sr^{2+}, La^{3+}) paired with transition-metal B-site ions (Fe^{3+}, Co^{3+}, Ni^{2+}, Mn^{3+}, Nb^{5+}, Ta^{5+}, W^{6+}, Ti^{4+}) within corner-sharing octahedra give rise to intertwined dielectric, piezoelectric, and conductive properties[5–8]. Beyond memory and sensing, these materials have also been explored for energy harvesting and photonic devices due to their tunable dielectric and optical responses[9, 10].

Among perovskite oxides, bismuth-based systems ($BiXO_3$, X = Fe, Mn, Al, Cr, Sc) are of special interest due to the presence of the $6s^2$ lone pair of Bi^{3+}, which induces strong lattice distortion and enhances ferroelectric polarization. $BiFeO_3$, for instance, exhibits a high Curie temperature (~830 °C) and large spontaneous polarization, making it one of the most extensively studied lead-free ferroelectrics[11–13]. However, its practical application is severely limited by high leakage currents arising from oxygen vacancies, mixed-valence Fe^{2+}/Fe^{3+} states, and the formation of secondary phases, such as $Bi_2Fe_4O_9$ and $Bi_{25}FeO_{39}$[14–16]. $BiMnO_3$, which becomes ferroelectric below about 550 K, likewise suffers from impurity formation (e.g., Bi_2O_3) that degrades its performance[17].

To mitigate these drawbacks, various synthesis and compositional-engineering approaches have been pursued. Rapid liquid-phase sintering and chemical leaching can suppress unwanted secondary phases[18,19], while targeted ion substitution at A- and B-sites allows precise control over defect chemistry and charge balance[20,21]. In particular, B-site engineering via Ni^{2+}, Co^{2+}, Mn^{3+}, and high-valence ions (Ti^{4+}, Se^{4+}) has proven effective in reducing vacancy concentrations and stabilizing cation valence, thereby lowering leakage currents and dielectric loss[22–25].

In our recently published study, it was demonstrated that Ti^{4+} substitution in $BiNi_{0.5}Ti_{0.5}O_3$ improved ferroelectric performance while significantly reducing conductivity[26]. Building on this foundation, the present work reports the solid-state synthesis of the selenium-substituted analogue

*Corresponding author: E-mail: alok.physics@nitmz.ac.in

$BiNi_{0.5}Se_{0.5}O_3$. Selenium (Se^{4+}) was selected for substitution at the Ni-site to control defect chemistry and suppress leakage conduction commonly observed in Bi-based perovskites. Se^{4+} possesses a higher valence state than Ni^{2+}, which helps in compensating oxygen vacancies and stabilizing charge balance in the lattice. This substitution is expected to reduce mixed-valence states and enhance dielectric stability. Similar high-valence B-site substitutions have been reported to improve electrical performance in Bi-based perovskite oxides[27]. This employ powder X-ray diffraction, scanning-electron microscopy, and energy-dispersive X-ray spectroscopy to confirm phase purity, microstructure, and stoichiometry; temperature and frequency-dependent dielectric, impedance, and electric-modulus measurements. Our results show that Se^{4+} incorporation further curtails leakage pathways and enhances ferroelectric switching, positioning $BiNi_{0.5}Se_{0.5}O_3$ as a promising candidate for advanced electronic and energy harvesting applications.

2 Materials and Methods

$BiNi_{0.5}Se_{0.5}O_3$ ceramics were fabricated via a conventional solid-state route. In addition to the conventional solid-state reaction route used in this study, $BiNi_{0.5}Se_{0.5}O_3$ can also be synthesized using alternative techniques such as the Sol-gel method, Citrate-nitrate combustion route, Hydrothermal synthesis, and Pechini method. These methods generally offer better compositional homogeneity and lower synthesis temperatures. However, the solid-state route was chosen for its simplicity, reproducibility, and suitability for bulk ceramic fabrication. High-purity Bi_2O_3, NiO, and SeO_2 powders were weighed according to the target stoichiometry and ground in an agate mortar for three hours under ambient conditions. The homogenized mixture was calcined at 950 °C for 4 h in air, then milled again to yield a fine, uniform powder. A small amount of polyvinyl alcohol (PVA) binder (≈1–2 wt %) was added before uniaxial pressing into pellets (11.5–12 mm diameter, 1.2 mm thickness) at 4×10^6 N m^{-2}. The "green" pellets were sintered in an oxygen-rich furnace at 980 °C for 4 h. The sintering temperature of 980 °C was optimized to achieve sufficient densification, enhanced grain growth, and improved electrical connectivity among grains while minimizing excessive selenium loss due to volatilization at still higher temperatures. The calcination temperature (950 °C) was selected to promote solid-state diffusion and phase formation of the constituent oxides, whereas sintering requires a slightly higher temperature to activate mass transport mechanisms such as lattice diffusion and grain-boundary diffusion. These processes are essential for pore elimination, grain-to-grain bonding, and mechanical integrity of the ceramic pellets. After cooling, silver electrodes were applied to both faces of each pellet and cured at 120 °C for 2 h to ensure reproducible contacts.

Phase purity and lattice parameters were determined by powder X-ray diffraction using a Rigaku Ultima-IV diffractometer (Cu Kα, $\lambda = 1.5405$ Å), scanning $2\theta = 20$-$80°$ with a step of 0.02° at 2°/min. Microstructural features were investigated by scanning electron microscopy (SEM, ZEISS). Elemental composition and homogeneity were confirmed via energy-dispersive X-ray spectroscopy (EDX). Dielectric and impedance measurements were performed using a Phase Sensitive Meter (PSM-1735, Newton 4th Ltd., UK) equipped with a programmable furnace, which allowed for variation of temperature and frequency. Parameters recorded included capacitance, dielectric constant, loss tangent, impedance, and electric modulus.

3 Results and Analysis

3.1 Structural and Microstructural Analysis

X-ray diffraction (XRD) analysis was carried out to determine the phase purity of the synthesized $BiNi_{0.5}Se_{0.5}O_3$ sample. The room-temperature XRD pattern is shown in Fig. 1 (a). The observed diffraction peaks are sharp and well-defined, indicating a favourable crystalline structure with good phase formation. XRD remains a widely used tool for structural characterization, with numerous computational programs available for analyzing both single-crystal and powder diffraction data. While single-crystal data offer precise structural insights depending on the crystal system and radiation source, powder diffraction primarily aids in phase identification and basic structural assessment. In this study, the software Jana2006[28], a well-established program for structural analysis, was employed to interpret the powder diffraction data and confirm phase composition. Due to limited prior knowledge of the exact crystal structure, a best-fit approach was adopted, emphasizing minimal discrepancies

between observed and calculated Bragg angles to refine phase identification. The diffraction pattern of $BiNi_{0.5}Se_{0.5}O_3$ was found to match two distinct phases. The presence of two phases in the XRD pattern arises from partial stabilization of secondary Bi-Se-rich phases during high-temperature solid-state synthesis. The Bragg positions, indicated by vertical markers, correspond to $Bi_{19.6}Ni_{6.4}O_{40}$ (space group: I23; lattice parameters: $a = b = c = 10.156$ Å), and BiSe (space group: P-3m1; lattice constants: $a = b = 4.203$ Å, $c = 22.795$ Å). The lattice parameters were refined using the Le Bail method, which optimizes peak positions and intensities. Iterative fitting was performed by adjusting microstructural parameters incrementally near their estimated values. A cosine Fourier series was applied for background modeling, and peak profiles were fitted using pseudo-Voigt functions. The refinement yielded a satisfactory fit, with a Goodness of Fit (GOF) of 8.83, Rp = 5.91, and wRp = 8.05. Selenium volatility and the complex phase stability of Bi-based oxides can lead to the formation of minor secondary phases such as BiSe along with the dominant perovskite-related phase ($Bi_{19.6}Ni_{6.4}O_{40}$). This multiphase nature is commonly reported in substituted bismuth oxides synthesized at elevated temperatures[27].

Figure 1 (b) presents the scanning electron microscopy (SEM) image along with the corresponding energy-dispersive X-ray spectroscopy (EDX) spectrum. The SEM image reveals a microstructure consisting of densely packed grains with a relatively uniform distribution. The grains exhibit polyhedral morphology with moderate size variation. Notably, intergranular porosity is evident, indicated by darker contrast regions observed at the grain boundaries. Grain size analysis was performed using ImageJ software, yielding an average grain size of approximately 3 μm, as determined by statistical evaluation. The elemental composition of the sample was determined using EDX analysis, also shown in Fig. 1 (b). The EDX spectrum confirms the presence of the principal Elements-Bi, Se, Ni, and O-with approximate weight percentages of 64 %, 6 %, 10.5 %, and 19.5 %, respectively. The corresponding atomic percentages are approximately 15.5 % for Bi, 5.5 % for Se, 9 % for Ni, and 70 % for O, closely matching the expected stoichiometry. The well-defined peaks and absence of impurity signals indicate the high purity and successful synthesis of the intended composition.

3.2 Dielectric Analysis

Dielectric spectra were acquired over the 1 kHz–1 MHz range at temperatures spanning 25 °C to 400 °C (Fig. 2 (a) and (b)) yielding the real permittivity (ε_r) and loss-tangent ($\tan\delta$) profiles. As shown in Fig. 2 (a), ε_r exhibits a marked decrease with increasing frequency at all temperatures at 25 °C it falls from ≈400 at 1 kHz to ≈205 at 1 MHz, while at 400 °C the decline is more pronounced (≈5222 to ≈353). This strong dispersion is characteristic of Maxwell-Wagner interfacial polarization arising from electrically heterogeneous region-conducting grains separated by resistive grain boundaries-which act as an effective two-layer dielectric[29, 30] in agreement with Koop's model[29]. Below ~10 kHz, space-charge accumulation at interfaces dominates, whereas above ~100 kHz ε_r approaches its static, high-frequency

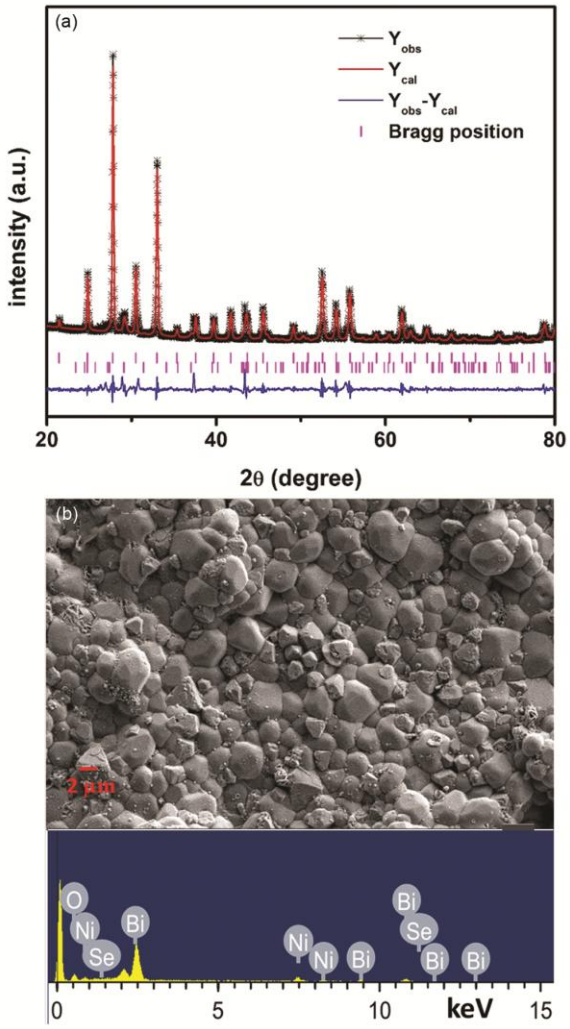

Fig. 1 — (a) XRD spectra of $BiNi_{0.5}Se_{0.5}O_3$ compound recorded at room temperature with matched phases; and (b) SEM image of $BiNi_{0.5}Se_{0.5}O_3$ compound along with EDX spectra

limit, reflecting the intrinsic dielectric response of the perovskite lattice.

Figure 2 (b) illustrates that tan δ is highest at low frequencies (e.g., ≈1.9 at 400 °C, 1 kHz) due to barrier-layer-capacitor effects at grain boundaries, which impose significant resistance and energy dissipation during long-range charge transport[30]. As frequency increases, dipolar relaxation and short-range hopping processes become predominant, driving tan δ down to a nearly constant baseline (≈ 0.3 at 1 MHz for 400 °C) and yielding minimal energy loss at high frequencies[29]. Increasing temperature shifts both ε_r and tan δ upward in the low-frequency regime, indicative of enhanced charge-carrier mobility and stronger interfacial polarization, but leaves their high-frequency plateaus virtually unchanged, underscoring the stability of the perovskite's intrinsic dielectric properties[29,30]. The clear separation between low-frequency interfacial dispersion and high-frequency intrinsic behavior suggests that, with optimized grain-boundary engineering to suppress tan δ, BiNi0.5Se0.5O3 holds promise for high-frequency dielectric and energy-storage applications. Figures 3 (a) and (b) shows the temperature-dependent ε_r and tan δ for various frequencies, respectively. The increasing trend of ε_r spectra is due to the increase in conductivity or the existence of space charge polarization in the as-prepared material.

3.3 Complex Impedance Analysis

To deconvolute the contributions of grains, grain boundaries, and electrode interfaces to the electrical response of $BiNi_{0.5}Se_{0.5}O_3$, complex impedance measurements were performed from 1 kHz to 1 MHz over the 25-400 °C range and displayed in Fig. 4. Figure 4 (a) shows that Z′ falls monotonically with increasing frequency at all temperatures. At 25 °C, Z′ decreases from ≈195 kΩ at 1 kHz to < 130 kΩ above 100 kHz, whereas at 250 °C, the low-frequency value

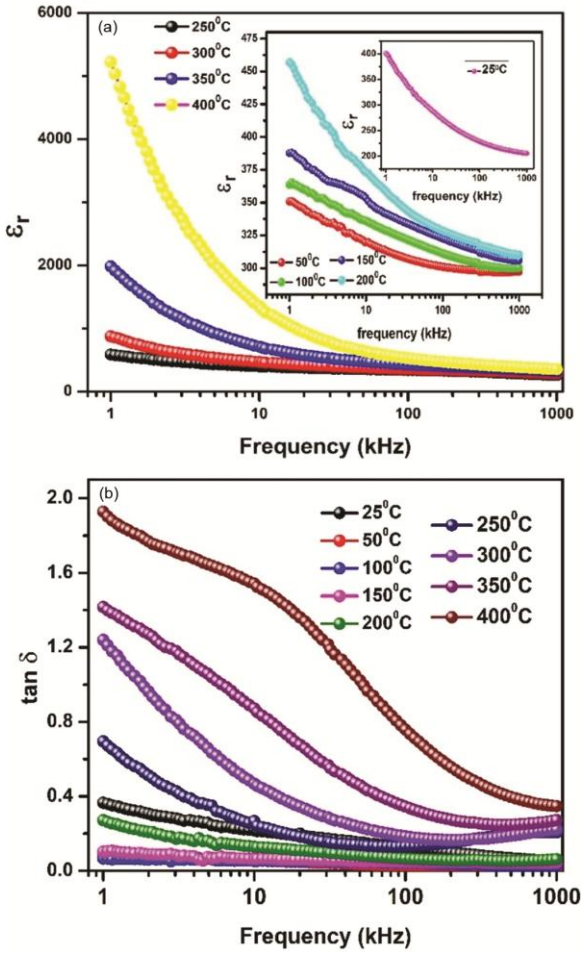

Fig. 2 — Dielectric parameters (a) Dielectric constant; and (b) tangent loss, as a function of the frequency of the compound $BiNi_{0.5}Se_{0.5}O_3$

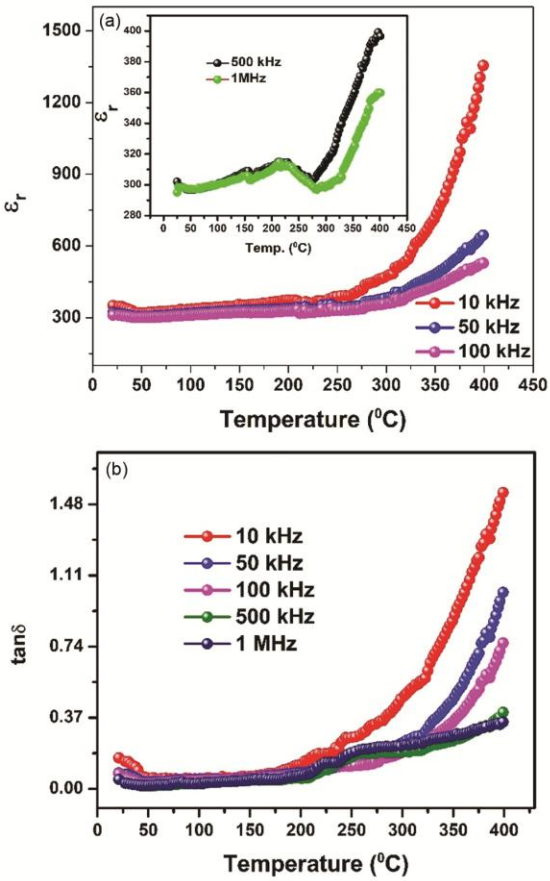

Fig. 3 — Dielectric parameters (a) Dielectric constant; and (b) tangent loss, as a function of the temperature of the compound $BiNi_{0.5}Se_{0.5}O_3$

peaks near 190 kΩ before declining on the same trajectory. Above ~200 kHz, Z′ curves converge, indicating that space-charge polarization at interfaces is fully relaxed and the response is dominated by the intrinsic lattice resistance[31]. The non-monotonic temperature dependence-Z′ diminishes from 25 to 100 °C, then rises at higher temperatures up to 250 °C -suggests that thermally activated carrier scattering at defect sites (e.g., oxygen vacancies, disordered grain boundaries) controls low-frequency conduction in this disordered perovskite[32]. After 250 °C, Z′ starts to decrease again, showing the disordered kind of semiconducting nature. The decrease in Z′ beyond 250 °C is attributed to thermally activated charge transport, where increased carrier mobility and defect-assisted hopping conduction dominate over grain boundary resistance. This behavior indicates a negative temperature coefficient of resistance (NTCR), typical of semiconducting oxides with disordered structures. As plotted in Fig. 4 (b), the magnitude of Z″ likewise diminishes with frequency. For temperatures ≥350 °C, a broad peak emerges, which shifts to lower frequencies and broadens with increasing temperature. This behavior reflects an Arrhenius-type increase in relaxation time, transitioning from long-range, interfacial polarization at low frequencies to defect-mediated dipolar hopping at high frequencies[33].

The Nyquist plot (Z″ vs Z′) study of $BiNi_{0.5}Se_{0.5}O_3$ over the temperature range of 25 °C to 400 °C provides meaningful insights into its charge transport mechanisms and is represented in Fig. 5 (a). An equivalent circuit of resistance and capacitance (representing grains and grain boundaries) was fitted using ZSimpWin 2.0[34]. From this model, grain and grain-boundary resistances, as well as constant-phase parameters, were extracted and are represented in Table 1, providing quantitative insight into the individual contributions that govern the electrical dynamics of $BiNi_{0.5}Se_{0.5}O_3$. At lower temperatures (25–250 °C), the Nyquist plots are accurately modeled using a single RQC equivalent circuit, indicating that the electrical response is mainly influenced by the

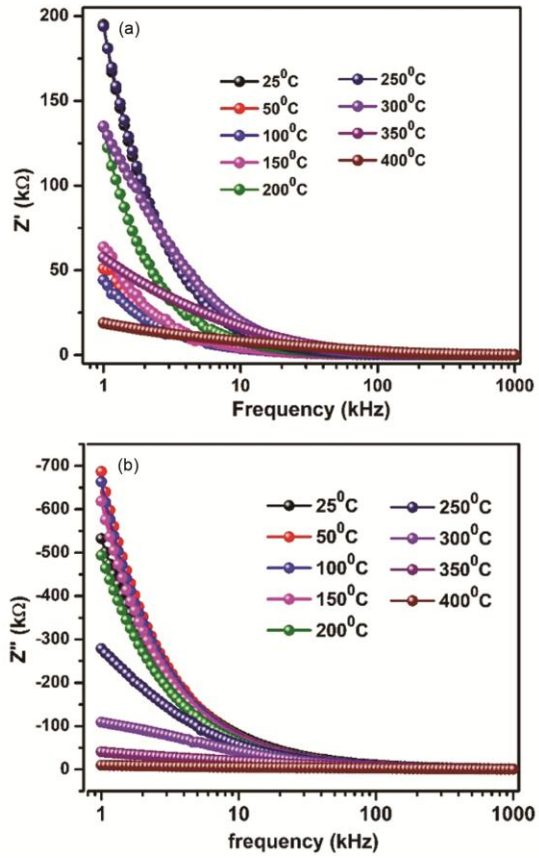

Fig. 4 — Variation of (a) real part of impedance (Z′); and (b) imaginary part of impedance (Z″) with frequency of the compound $BiNi_{0.5}Se_{0.5}O_3$

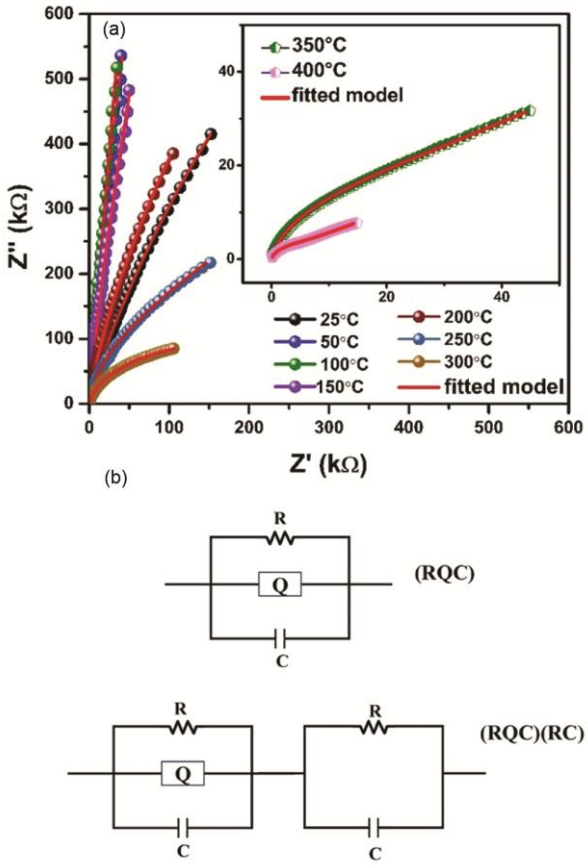

Fig. 5 — (a) Nyquist plot of the compound $BiNi_{0.5}Se_{0.5}O_3$; and (b) Equivalent circuit model employed for fitting the Nyquist impedance data of the $BiNi_{0.5}Se_{0.5}O_3$ ceramic

Table 1 — Equivalent fitted circuit from Nyquist plot with the value of capacitance and resistance values for different regions

Temperature (°C)	Model	R_g (Ω)	Q	C_g (F)	R_{gb} (Ω)	C_{gb} (F)
25	(RQC)	1.998E7	3.319E-9	1.19E-10	-	-
50	(RQC)	2.716E17	5.048E-10	1.846E-10	-	-
100	(RQC)	3.124E18	2.747E-10	1.647E-10	-	-
150	(RQC)	1.039E7	3.486E-10	1E-18	-	-
200	(RQC)	6.589E6	1.624E-9	1.853E-10	-	-
250	(RQC)	6.812E5	8.267E-10	1.06E-11	-	-
300	(RQC)(RC)	2.694E5	2.663E-9	3.964E-18	2.924E4	7.395E-10
350	(RQC)(RC)	7.468E14	6.969E-7	2.356E-10	176.8	4.408E-10
400	(RQC)(RC)	6.126E4	7.22E-7	1.894E-10	2135	1.111E-9

bulk (grain) region of the material[35]. A noticeable decrease in grain resistance (R_g), from approximately $1.998 \times 10^7\ \Omega$ at 25 °C to $6.8 \times 10^5\ \Omega$ at 250 °C, reflects the thermally activated nature of conduction within the grains. Both the bulk capacitance (C_g) and the constant phase element (Q) show relatively small changes, suggesting stable dielectric behavior in the grain interiors, albeit with slight deviations from ideal capacitive behavior. As the temperature rises beyond 300 °C, the electrical response becomes more complex, necessitating a combination of RQC and RC circuits for accurate modeling. This shift points to the growing influence of grain boundary effects in addition to bulk contributions. The grain boundary resistance (R_{gb}) drops significantly, while the grain boundary capacitance (C_{gb}) increases, indicating a build-up of interfacial polarization[36]. These changes suggest a transition from single-region to dual-region conduction with temperature, characteristic of semiconducting oxides, and imply the increasing role of Maxwell-Wagner-type interfacial relaxation at higher temperatures. The equivalent circuit model used for fitting the Nyquist impedance data is shown in Fig. 5 (b).

3.4 Electric Modulus Analysis

To decouple bulk relaxation from interfacial and electrode effects in $BiNi_{0.5}Se_{0.5}O_3$, the complex electric modulus

$$M^* = M' + jM'' \quad \ldots (1)$$

And the real part and imaginary part can further be expressed as,

$$M' = A\left[\frac{(\omega RC)^2}{1+(\omega RC)^2}\right] \text{ and } M'' = A\left[\frac{\omega RC}{1+(\omega RC)^2}\right] \quad \ldots (2)$$

was evaluated[37]. Here, M′(ω) (the real part) and M″(ω) (the imaginary part) provide complementary insights into dipolar dynamics and charge-carrier motion[38].

Figure 6 (a) plots M′(ω) from 1 kHz to 1 MHz at temperatures of 25-400 °C. At low frequencies (< 1 kHz), M′ is effectively zero for all temperatures, indicating that electrode polarization is negligible and that long-range charge transport is uninhibited by interfacial barriers. As ω increases into the mid-frequency domain (~1–100 kHz), M′ rises steeply, marking the onset of bulk dipolar relaxation. Above ~100 kHz, all curves converge to a plateau, corresponding to the high-frequency, intrinsic modulus of the Se-substituted perovskite. With increasing temperature, the inflection point of the sigmoidal rise shifts to higher frequencies, reflecting thermally activated acceleration of dipole reorientation within the lattice.

In Fig. 6 (b), each M″(ω) spectrum displays a broad, temperature-dependent peak whose maximum frequency (f_{max}) and width increase with temperature. The low-frequency side of each peak corresponds to extended, long-range hopping of charge carriers, whereas the high-frequency flank reflects localized, short-range dipolar motion within potential wells[38,39]. Peak broadening at elevated temperatures further signifies a distribution of relaxation times, characteristic of non-Debye behaviour arising from structural disorder such as oxygen vacancies and grain-boundary heterogeneities. The electric-modulus formalism thus effectively suppresses extrinsic artifacts and highlights a single, thermally activated relaxation process in $BiNi_{0.5}Se_{0.5}O_3$. The systematic shift of both M′ dispersion and M″ peak frequencies with temperature underscores the central role of defect-mediated charge hopping in the material's AC dielectric response.

3.5 AC-Conductivity Analysis

The frequency- and temperature-dependent AC conductivity (σ_{ac}) of $BiNi_{0.5}Se_{0.5}O_3$ was measured between 1 kHz and 1 MHz over the 25-400 °C range

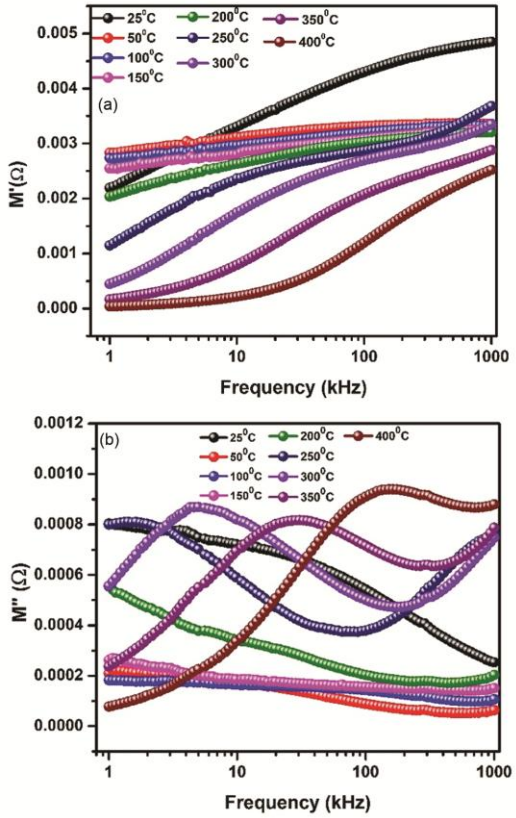

Fig. 6 — Variation of (a) real part ($M^{'}$); and (b) imaginary part ($M^{''}$) of electric modulus with respect to change in frequency of the compound $BiNi_{0.5}Se_{0.5}O_3$

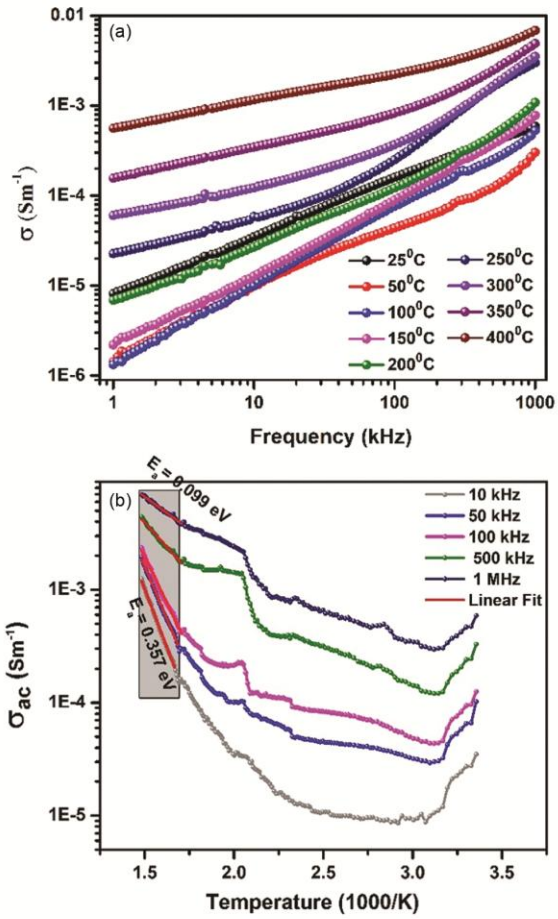

Fig. 7 — ac conductivity variation with respect to (a) varying frequency; and (b) with varying inverse of absolute temperature of the compound $BiNi_{0.5}Se_{0.5}O_3$

(Fig. 7 (a)). At each temperature, σ_{ac} increases monotonically with frequency, defining two distinct regimes. Below a characteristic crossover frequency, σ_{ac} is essentially frequency-independent (σ_{dc}), whereas above this threshold it follows Jonscher's universal power law[40],

$$\sigma_{ac} = \sigma_{dc} + A\omega^{n} \quad \ldots (3)$$

Here, a quantifies the strength of polarization and the exponent n ($0 < n < 1$) decreases slightly with rising temperature, indicative of a thermally activated hopping mechanism among localized states.

Figure 7 (b) depicts Arrhenius plots of σ_{ac} versus 1000/T at selected frequencies. In the high-temperature region, linear fits to[41],

$$\sigma = \sigma_0 exp\left(-\frac{E_a}{K_B T}\right) \quad \ldots (4)$$

yield activation energies E_a, shown in Table 2, that diminish from roughly 0.357 eV at 10 kHz to 0.099 eV at 1 MHz. This frequency-dependent reduction in Ea reflects the fact that higher-frequency fields facilitate shorter-range polaron hopping, thereby lowering the energy barrier for carrier motion across defect sites[42]. Together, the two-regime behavior in Fig. 7 (a) and the NTCR (negative temperature coefficient of resistance) evident in Fig. 7 (b) confirm that AC conduction in $BiNi_{0.5}Se_{0.5}O_3$ is governed by a combination of frequency-independent DC transport at low frequencies and dispersive, hopping-dominated processes at higher frequencies, with an overall semiconducting character.

Table 2 — Calculated activation energy from different regions of temperature-dependent ac conductivity

Frequency	E_a (eV)
10 kHz	0.357
50 kHz	0.320
100 kHz	0.283
500 kHz	0.149
1 MHz	0.099

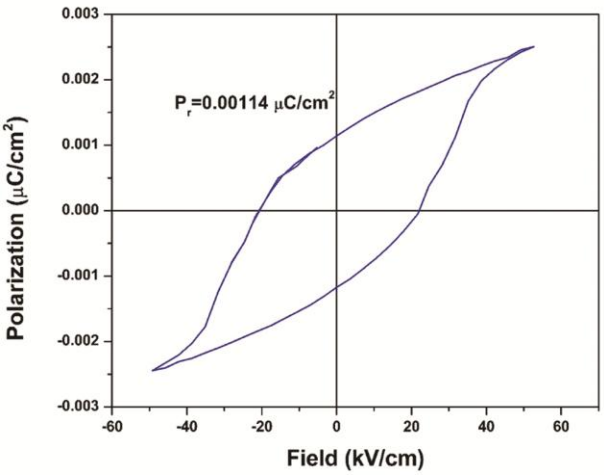

Fig. 8 — P-E curve of $BiNi_{0.5}Se_{0.5}O_3$ ceramic

3.6 Ferrroelectric Analysis

The polarization-electric field (P-E) hysteresis loop of the $BiNi_{0.5}Se_{0.5}O_3$ ceramic measured at room temperature is shown in Fig. 8. The loop exhibits a slim, elongated hysteresis profile, indicating the presence of weak ferroelectric or polar behavior with a significant contribution from leakage current and conduction-related effects. The measured remanent polarization (P_r) is approximately 0.00114 μC/cm^2 with coercive field (E_c) 21.7117 kV/cm and maximum polarization (P) of 0.0025 μC/cm^2, which are relatively small compared to classical ferroelectric perovskites but are typical for Bi-based substituted oxides synthesized via solid-state routes[37]. The unsaturated nature of the loop, even at a maximum applied electric field, suggests that complete domain switching is not achieved under the present measurement conditions. This behavior can be attributed to the presence of charge carriers associated with defects such as oxygen vacancies, mixed-valence states, and grain-boundary effects, which are known to influence the electrical response of Bi-based ceramics.

4 Conclusion

$BiNi_{0.5}Se_{0.5}O_3$ was successfully synthesized via a conventional solid-state reaction route, yielding a multiphase perovskite ceramic with well-defined grains (~3 μm). Structural analysis confirmed phase formation, while dielectric measurements revealed a high permittivity ($\varepsilon_r \approx 5222$ at 400 °C and 1 kHz). Both ε_r and $\tan\delta$ showed the expected frequency-dependent decrease, along with a clear positive temperature coefficient. Complex impedance spectroscopy identified separate grain and grain boundary contributions and confirmed a negative temperature coefficient of resistance. Equivalent circuit modeling quantified the respective resistive and capacitive elements in the system. AC conductivity followed Jonscher's universal power law, revealing a thermally activated hopping mechanism at low temperatures that transitions to oxygen-vacancy-mediated transport at higher temperatures. A frequency-dependent decrease in activation energy further supports the presence of polaron hopping and defect-assisted conduction mechanisms. The slim and unsaturated P-E hysteresis loop with low polarization values indicates weak ferroelectric or polar behavior in $BiNi_{0.5}Se_{0.5}O_3$, with the electrical response predominantly governed by defect-induced leakage conduction rather than complete ferroelectric domain switching. Collectively, these findings establish $BiNi_{0.5}Se_{0.5}O_3$ as a promising candidate for next-generation capacitors, multilayer ceramic components, and high-frequency energy storage applications. Future studies will focus on tailoring the microstructure and evaluating device integration to fully exploit its multifunctional performance.

References

1 Hu B, Fan H, Ning L, Gao S, Yao Z & Li Q, *Ceram Int*, 44 (2018) 10968.
2 Yang L, Kong X, Li F, Hao H, Cheng Z, Liu H, Li J F & Zhang S, *Prog Mater Sci*, 102 (2019) 72.
3 Whittingham M S, *MRS Bull*, 33 (2008) 411.
4 Yan B, Fan H, Wang C, Zhang M, Yadav A K, Zheng X, Wang H & Du Z, *Ceram Int*, 46 (2020) 281.
5 Setter N, Damjanovic D, Eng L, Fox G, Gevorgian S, Hong S, Kingon A, Kohlstedt H, Park N Y, Stephenson G B, Stolitchnov I, Taganstev A K, Taylor D V, Yamada T, & Streiffer S, *J Appl Phys*, 100 (2006) 051606.
6 Zhou W, Deng H, Yang P & Chu J, *Appl Phys Lett*, 105 (2014) 111904.
7 Shi T, Li G & Zhu J, *Ceram Int*, 43 (2017) 2910.
8 Lisnevskaya I V, Lupeiko T G & Bikyashev E A, *Russ J Inorg Chem*, 60 (2015) 140.
9 Fan P, Liu K, Ma W, Tan H, Zhang Q, Zhang L, Zhou C, Salamon D, Zhang S T, Zhang Y, Nan B & Zhang H, *J Materiomics*, 7 (2021) 508.
10 Zhao C, Huang Y & Wu J, *InfoMat*, 2 (2020) 1163.
11 Selbach S M, Tybell T, Einarsrud M A & Grande T, *Adv Mater*, 20 (2008) 3692.
12 Gheorghiu F P, Ianculescu A, Postolache P, Lupu N, Dobromir M, Luca D & Mitoseriu L, *J Alloys Compd*, 506 (2010) 862.
13 Moreau J M, Michel C, Gerson R & James W J, *J Phys Chem Solids*, 32 (1971) 1315.
14 Neaton J B, Ederer C, Waghmare U V, Spaldin N A & Rabe K M, *Phys Rev B Condens Matter Mater Phys*, 71 (2005) 014113.

15 Wang D, Khesro A, Murakami S, Feteira A, Zhao Q & Reaney I M, *J Eur Ceram Soc*, 37 (2017)1857.
16 Zhou C, Yang H, Zhou Q, Cen Z, Li W, Yuan C & Wang H, *Ceram Int*, 39 (2013) 4307.
17 Hanif S, Hassan M, Riaz S, Atiq S, Hussain S S, Naseem S & Murtaza G, *Results Phys*, 7 (2017) 3190.
18 Qin H, Zhang H, Zhang B P & Xu L, *J Am Ceram Soc*, 94 (2011) 3671.
19 Zhou C, Yang H, Zhou Q, Cen Z, Li W, Yuan C & Wang H, *Ceram Int*, 39 (2013) 4307.
20 Wani W A, Kundu S, Ramaswamy K & Venkataraman H, *J Alloys Compd*, 846 (2020) 156334.
21 Jena A K, Satapathy S & Mohanty J, *J Appl Phys*, 124 (2018).
22 Dong G, Tan G, Luo Y, Wang T, Ren H & Xia A, *J Alloys Compd*, 654 (2016) 419.
23 Cai W, Fu C, Gao R, Jiang W, Deng X & Chen G, *J Alloys Compd*, 617 (2014) 240.
24 Sharma G N, Dutta S, Singh S K & Chatterjee R, *Mater Res Express*, 3 (2016) 106202.
25 Deng X, Wang W, Gao R, Cai W, Chen G & Fu C, *J Mater Sci Mater Electron*, 29 (2018) 6870.
26 Lalngilneia P C, Joshi S, Shukla A, Kumara N & Choudhary R N P C, *Trans Ind Ceram Soc*, 84 (2) (2025) 151.
27 Chu S, Zhang M, Deng H, Wang Z, Wang Y, Pan Y, Yan H, *J Alloys Compd*, 689 (2016) 475.
28 Petrícek V, Dušek M & Palatinus L, *J Crystallogr*, 229 (2014) 345.
29 Koops C G, *Phys Rev*, 83 (1951)121.
30 Patankar K K, Dombale P D, Mathe V L, Patil S A & Patil R N, *Mater Sci Eng B*, 87 (2001) 53.
31 Wagner K W, *Arch Electr Eng*, 2 (1914) 371.
32 Mohanty S, Choudhary R N P, Padhee R & Parida B N, *Ceram Int*, 40 (2014) 9017.
33 Amin M, Rafique H M, Yousaf M, Ramay S M & Atiq S, *J Mater Sci Mater Electron*, 27 (2016) 11003.
34 Kumar N, Shukla A, Kumar N, Sahoo S, Hajra S & Choudhary R N P, *Ceram Int*, 44 (2018) 21330.
35 Kumar N, Shukla A & Choudhary R N P, *J Mater Sci Mater Electron*, 28 (2017) 6673.
36 Rani S, Sanghi S, Agarwal A, Kumar R & Singh O, *Appl Phys A Mater Sci Process*, 128 (2022)1.
37 Joshi S, Shukla A, Kumar N & Choudhary R N P, *Ceram Int*, 50 (2024) 1643.
38 Alimuddin M H, Kumar S, Ali S, Koo B H, Chung H & Kumar R, *J Alloys Compd*, 511 (2012) 107.
39 Rafiq M A, Rafiq M N & Saravanan K V, *Ceram Int*, 41 (2015) 11436.
40 Jonscher A K, *Nature*, 267 (1977) 673.
41 Halder S, Parida K, Das S N, Pradhan S K, Bhuyan S & Choudhary R N P, *Phys Lett A*, 382 (2018) 716.
42 Kumar N, Shukla A, Kumar N, Hajra S, Sahoo S & Choudhary R N P, *J Mater Sci Mater Electron*, 30 (2019) 1919.